



Differences in the permeability assessment of the fractured reservoir rocks using the conventional and the rough discrete fracture network modeling

Di Shi^{1,2} · Xin Chang^{2,3} · Liping Li¹ · Mingyang Wu^{2,3} · Rui Song^{2,3} · Yintong Guo^{2,3} · Jupeng Tang¹ · Jianjun Liu^{2,3}

Received: 9 June 2023 / Accepted: 9 November 2023 / Published online: 11 December 2023
© The Author(s) 2023

Abstract

Permeability assessment of naturally fractured rocks and fractured rocks after fracturing is critical to the development of oil and gas resources. In this paper, based on the discrete fracture network (DFN) modeling method, the conventional discrete fracture network (C-DFN) and the rough discrete fracture network (R-DFN) models are established. Through the seepage numerical simulation of the fractured rocks under different DFN, the differences in permeability of the fractured rocks under different parameters and their parameter sensitivity are analyzed and discussed. The results show that unconnected and independent fractures in the fracture network may weaken the seepage capacity of the fractured rocks. The fractured rock permeability increases with increase in connectivity and porosity and decreases with increase in maximum branch length and fracture dip. The use of C-DFN to equate the fracture network in the fractured rocks may underestimate the connectivity of the fracture network. For the more realistic R-DFN, the promotion of gas flow by connectivity is dominant when connectivity is high, and the hindrance of gas flow by fracture roughness is dominant when connectivity is low or when it is a single fracture. The permeability of the fractured rocks with R-DFN is more sensitive to the parameters than that of the fractured rocks with C-DFN. The higher the connectivity and porosity of the fractured rocks, the more obvious the difference between the permeability of the fractured rocks evaluated by C-DFN and R-DFN.

Keywords Fractured rocks · Permeability · Discrete fracture network · Connectivity · Rough fractures

Abbreviations

C-DFN	Conventional discrete fracture network
DFN	Discrete fracture network
DFNs	Discrete fracture networks
Eq.	Equation
Eqs.	Equations
R-DFN	Rough discrete fracture network

List of symbols

C	Set of the cumulative number of subscripts of different growth vectors
c	Topological connectivity
c_j	Cumulative number of the j th growth vector
D	Set of its growth vectors
D_f	Fractal dimension of the fracture network
D_{Tf}	Tortuosity fractal dimension
d_j	j Th growth vector
F	Set of a rough fracture
f_1	Starting point
f_i	Coordinate of the i th point
f_n	Ending point
f_{random}	Random fracture starting point
K	Total permeability of the fractured rocks, m^2
K_f	Fracture network permeability, m^2
K_{fC}	Conventional flat panel fracture network permeability, m^2
K_{fR}	Rough fracture network permeability, m^2
K_p	Matrix permeability, mD
L_0	Characteristic length, m

✉ Xin Chang
xchang@whrsm.ac.cn

¹ School of Mechanics and Engineering, Liaoning Technical University, Fuxin 123000, Liaoning, China

² State Key Laboratory of Geomechanics and Geotechnical Engineering, Institute of Rock and Soil Mechanics, Chinese Academy of Sciences, Wuhan 430071, China

³ Hubei Key Laboratory of Geo-Environmental Engineering, Institute of Rock and Soil Mechanics, Chinese Academy of Sciences, Wuhan 430071, China

L_F	True length (rough tortuous fracture length), m
L_{Macro}	Macroscopic length of the fracture, (conventional straight fracture length), m
l_{bmax}	Maximum branching length, m
l_{bmin}	Minimum branching length, m
N_I	Number of the <i>I</i> -nodes
N_X	Number of the <i>X</i> -nodes
N_Y	Number of the <i>Y</i> -nodes
ΔP	Pressure gradient, Pa
V	Set of disordered growth vectors
V	Gas flow rate, m/s
v_i	Local growth vector
V_{Macro}	Macroscopic growth vector
V_S	Set of ordered growth vectors
β	Aperture proportionality coefficient
θ	Fracture dip angle, °
τ	Tortuosity
λ	Gas molecular free range, m
μ	Gas viscosity, Pa·s
ρ_g	Gas density, kg/m ³
ϕ	Porosity
$\zeta_{im}(x, y)$	Model matrix image function value

Introduction

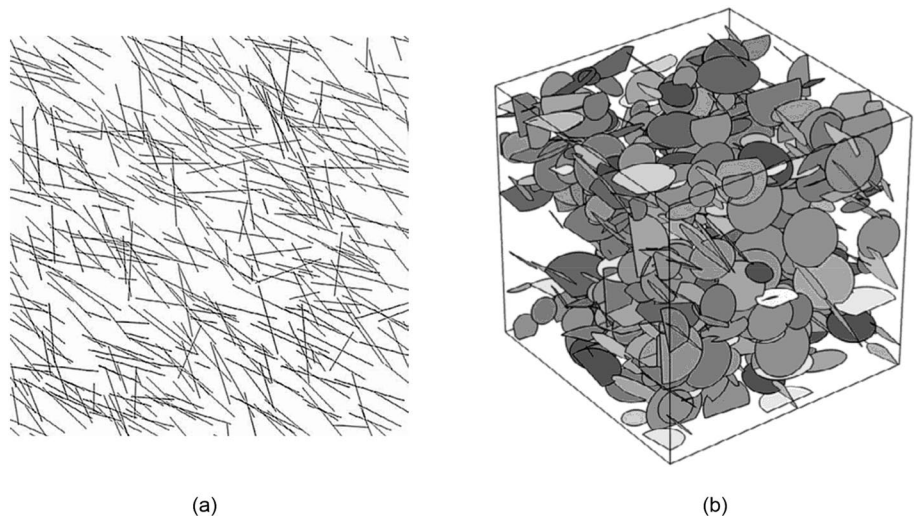
Due to the demand for unconventional oil and gas reservoirs energy development, fracture modification of reservoirs is often required (Nguyen et al. 2022; Lin et al. 2021; Lavrov 2021). Reservoir modification makes the natural and artificial fractures in the reservoir gradually expand, thus forming a complex network of interconnected fractures. Fractures provide a dominant channel for fluid flow in a reservoir and are considered a key property affecting reservoir permeability (Jia et al. 2022; Abdelazim 2020; Zarin et al. 2023). Reservoir permeability is critical for

engineering fields such as oil and gas extraction, subsurface energy storage and geothermal energy development. Therefore, assessing the fractured rock permeability by characterizing the fracture network and thus predicting the reservoir permeability has been an important research direction in reservoir development (Hosseinzadeh et al. 2023; Ji et al. 2023).

The traditional fracture network model assumes that the fractures are parallel panels embedded in the rocks and the fluid flows between the flat planes, which is called the parallel panel model (Hosseini et al. 2021; Li et al. 2019). Based on this assumption, some researchers have developed discrete fracture network (DFN) models (Fig. 1) in two-dimensional planes and three-dimensional spaces according to the statistical characteristics and distribution laws of reservoir fractures (Ringel et al. 2021; Dong et al. 2019). In these models, randomly distributed linear fractures or flat fractures constitute fracture networks with different morphologies. In this case, the fractured rock permeability is generally evaluated using the cubic law (Witherspoon et al. 1980) according to the characteristic parameters characterizing the fracture network (Wu et al. 2020; Yang et al. 2021). With the application of fractal theory (Mandelbrot 1982; Yu and Li 2011) in fracture characterization, the study of bifurcation fracture network characterization and its permeability based on reservoir fracture extension has gradually gained attention (Khodaei et al. 2021). However, in most research on bifurcation fractures, it is still assumed that the fractures at all levels are flat or linear fractures. This is not consistent with the real morphology of fractures in actual reservoirs.

In reality, the fracture of a reservoir is not a straight line or a flat panel, but often undulates along the strike, and its real form is tortuous and rough (Ni et al. 2021; Wu et al. 2021; Sun et al. 2023). However, the characteristics and structure of fracture networks in real reservoirs are

Fig. 1 **a** Two-dimensional and **b** three-dimensional conventional discrete fracture network models (Li et al. 2020)



very complex. Embodying the roughness characteristics of fractures is very difficult for constructing complex fracture networks. As a result, a series of studies have been developed on the characterization of rough fractures, such as point cloud data processing by fracture rock morphology scanning so as to reconstruct rough fracture surfaces (Daghighi et al. 2022; Lu et al. 2022), characterization and assessment of fracture surfaces roughness using the *JRC* method (Abe and Deckert 2021), numerical simulation of fractures using numerical manifold method (Ning et al. 2022; Hu and Rutqvist 2022), etc. Also, in studies assessing the fractured rock permeability, researchers have incorporated the fracture roughness, such as assuming the fractures as tortuous circular tubes or tortuous traces with fractal characteristics for theoretical derivation (Gao et al. 2021), setting the roughness coefficients of the fractures in the DFN model (Yao et al. 2020), generating fractal surfaces with different roughness (Wang et al. 2022) for numerical simulation, etc. Recently, a pixel fracture reconstruction method that can be used for fracture evolution simulation has been proposed (Wu et al. 2020). Using this method, the real fracture surface of the rock can be successfully reconstructed for fracture geological model reconstruction, and the fractal dimension of the real fracture surface can be reasonably evaluated (Wu et al. 2021). In addition, based on this reconstruction method, the stochastic DFN model (Xia et al. 2021) and real fractured coal rock model (Luo et al. 2021) that conform to the reservoir fracture statistics have been developed.

In the above study, fracture length is one of the key parameters necessary to assess the fractured rock permeability. However, the fracture length in the network is not unique because the terminating end of the fracture trace is often difficult to determine. Therefore, branch lengths in topology theory are introduced to avoid this uncertainty (Lahiri 2021). In addition, topology theory can also characterize the difference in the connectivity of the fracture network due to the different fracture structures (Sanderson and Nixon 2018; Ji et al. 2023). Topological connectivity is expressed as the ratio of the number of connected fractures to the total number of fractures, whereas branch length refers to the fracture segments connecting any two nodes in a fracture network. Topological connectivity and branch length together reflect the degree of connectivity of a network. Therefore, using topological theory, permeability equations and DFN models based on geometric and structural parameters of fracture networks have been developed to assess the fractured rock permeability (Lahiri 2021; Zhu et al. 2021; Zhang et al. 2022). However, although many permeability assessment models have been proposed and developed based on fractal and topology theories (Shi et al. 2023, 2022; Wu et al. 2022; Al-Dujaili et al. 2021; Fang et al. 2023; Luo et al. 2023), the differences between

different fracture network models in the permeability assessment of fractured rocks are rarely mentioned.

In this paper, conventional DFN (C-DFN) and rough DFN (R-DFN) models are established by using the DFN modeling method. The theoretical model of permeability from previous studies is embedded in COMSOL, and the simulation results of the permeability of fractured rocks with different DFNs are compared by numerical simulation of seepage in fractured rocks. Moreover, the differences in the permeability assessment of conventional and rough fractured rocks and their sensitivity to different parameters are analyzed. Subsequently, the differences in fracture network connectivity and permeability of fractured rocks under different DFNs are discussed.

Numerical simulation of seepage in fractured rocks with C-DFN or R-DFN

Modeling theory for different DFNs

To construct a fracture network in the two-dimensional plane, it is first necessary to solve the problem of quantitative characterization and stochastic reconstruction of individual fractures. For rough fractures, Barton (Barton 1973) found the *JRC* (joint roughness coefficient) parameter values of rock fractures and the corresponding ten standard fracture morphology images. As an example, the standard joint profiles for $JRC = 8-10$ are shown in Fig. 2a. Enlarging this joint profile, it can be seen that the rough fracture can be regarded as consisting of $(n-1)$ line segments connected by n discrete points f (solid red circles) in an orderly manner, as in Fig. 2b. In Fig. 2b, F denotes a rough fracture, f_i is the coordinate of the i th point, and the starting and ending points are f_1 and f_n , respectively. Therefore, when the ordered discrete points are determined, a completely determined rough fracture can be obtained. At this point, for the whole rough fracture, a path with direction and length (blue arrow) can be formed from its starting point to the endpoint. This path indicates the macroscopic direction of the whole rough fracture. It is named here as the macroscopic growth vector V_{Macro} . And the path with direction and length connecting the discrete points f_i and f_{i+1} indicates the microscopic direction of the rough fracture locally, thus naming it as the local growth vector v_i . For conventional fracture assumption in the two-dimensional plane, the path and direction of its linear fracture are often consistent with this macroscopic growth vector, i.e., the fracture is assumed to be a straight line connecting the starting point f_1 and the ending point f_n . Comparison with Fig. 2a reveals that this assumption is clearly lacking in fidelity. Assuming that the discrete point f_i has coordinates (x_i, y_i) in the two-dimensional coordinate plane, the macroscopic growth vector V_{Macro} of this rough

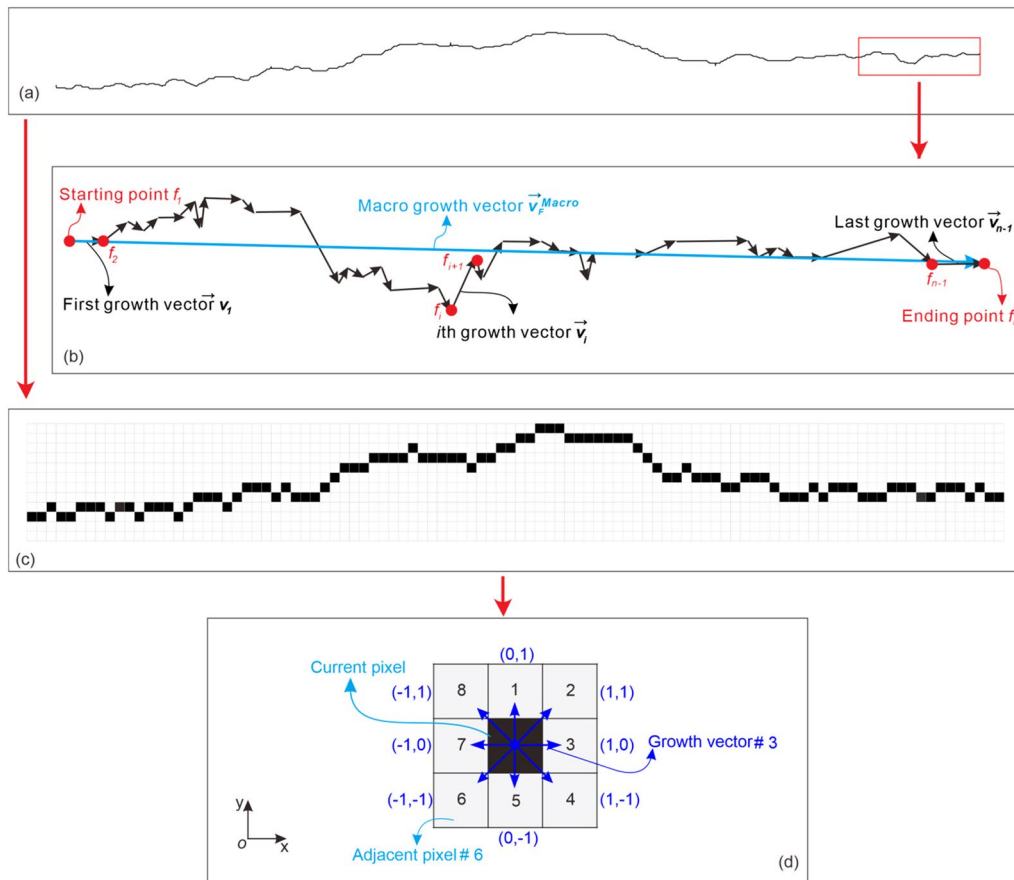


Fig. 2 **a** Standard joint profile curve (JRC=8–10), **b** Quantitative characterization based on vector statistics, **c** Pixel point of a rough fracture in a two-dimensional plane, **d** Eight-neighborhood determination and eight growth vectors

fracture and the local growth vector \vec{v}_i of the i th segment can be given by the following equation, respectively:

$$\vec{V}_{Macro} = (x_n - x_1, y_n - y_1), \quad (1)$$

$$\vec{v}_i = (x_{i+1} - x_i, y_{i+1} - y_i), \quad (2)$$

Thus, for the two modes of conventional and rough fractures, the macroscopic length L_{Macro} of the fracture (conventional straight fracture length) and its true length L_F (rough tortuous fracture length) can be expressed as follows, respectively.

$$L_{Macro} = \sqrt{(x_n - x_1)^2 + (y_n - y_1)^2}, \quad (3)$$

$$L_F = \sum_{i=1}^{n-1} \sqrt{(x_{i+1} - x_i)^2 + (y_{i+1} - y_i)^2}, \quad (4)$$

Thus, a set of ordered growth vectors $\vec{V}_S = \{\vec{v}_i\}$ ($i = 1, 2, 3, \dots, n-1$) can be obtained with respect to this rough

fracture. At this point, a rough fracture can be identified by the starting point f_1 and the set \vec{V}_S of ordered growth vectors. And the conventional fracture corresponding to this rough fracture can be determined by the macroscopic vectors, i.e., the starting point f_1 and the ending point f_n of the rough fracture.

It can be observed from Fig. 2b that if the order of the local growth vectors \vec{v}_i is changed, rough fractures with different morphologies are formed, but the statistical classes and numbers of these rough fracture growth vectors are the same. Thus, identical similar rough fractures with the same vector statistics can be uniformly represented as $\vec{F}_R = (f_{random}, \vec{V}) = (f_{random}, \{\vec{v}_i\})$, $i \in [1, 2, \dots, n-1]$. The corresponding similar conventional fractures $\vec{F}_C = (\{f_1\}, \{f_n\})$, $n \in [1, 2, \dots, n]$, where f_{random} is the random starting point, \vec{V} is the set of disordered growth vectors, and f_1 and f_n are the sets of disordered starting and ending points, respectively. At this point, once the set of growth vectors is determined, a similar class of rough fractures and conventional fractures can be obtained. However, if the original order of the growth vectors is not considered, when the number of growth vectors $n \rightarrow \infty$, the quantitative characterization using \vec{F}_R requires

a huge amount of data and storage resources. Therefore, it is also necessary to limit the number of different growth vectors in order to accommodate practical applications.

In the two-dimensional pixel plane, a rough fracture consisting of multiple line segments can be regarded as multiple pixels connected sequentially, as shown in Fig. 2c. At this point, any pixel point of the fracture has at most 8 neighboring pixels and there exist eight possible growth vectors (Wu et al. 2023), as in Fig. 2d. As a result, the growth vectors can be limited. The set \mathbf{D} of its growth vectors can be expressed as

$$\mathbf{D} = \{\mathbf{d}_j\} = \left\{ \begin{array}{cccccccc} 0 & 1 & 1 & 1 & 0 & -1 & -1 & -1 \\ 1 & 1 & 0 & -1 & -1 & -1 & 0 & 1 \end{array} \right\}, \quad (5)$$

where \mathbf{d}_j denotes the j th growth vector.

Then, in the two-dimensional pixel plane, identical similar rough fractures $\mathbf{F}_R = (f_{\text{random}}, \{v_i\})$, $i \in [1, 2, \dots, n-1]$, where $v_i \in \mathbf{D}$, i.e., any growth vector v_i of a rough fracture can be found in set \mathbf{D} of different growth vectors. After determining the set of different growth vectors, it is possible to characterize identical similar rough fractures in the two-dimensional pixel plane as long as the set \mathbf{D} of different growth vectors and the set \mathbf{S} of growth vector subscripts are determined. Following this, the corresponding conventional fractures can also be characterized. Since the different growth vectors in the pixel plane are known, the number of identical repeated subscripts can be obtained statistically to obtain the set $C = \{c_j\}$ of the cumulative number of subscripts of different growth vectors, where c_j denotes the cumulative number of the j th growth vector ($j = 1, 2, \dots, 8$). Thus, identical similar rough fractures in the two-dimensional pixel plane can be characterized by using the following equation:

$$\mathbf{F}_S = (f_{\text{random}}, \mathbf{D}, C), \quad (6)$$

According to Eq. (6), it is necessary to determine the growth vector \mathbf{d}_j and its corresponding cumulative number of subscripts c_j for each fracture when generating multiple rough fractures with the same statistical characteristics in a specific pixel plane, where \mathbf{d}_j can be obtained from Eq. (5). Therefore, to establish the DFN, the first step is to obtain the set C of the cumulative number of different growth vector subscripts. The curves and point sets of ten standard joint profiles (Barton 1973) can be obtained by image processing techniques and mathematical morphology methods (Wu et al. 2020). In this paper, this method is used to obtain the point sets of the joint profiles and to determine set C of the cumulative number of growth vectors of the fracture points along the eight directions. Therefore, firstly, the Python program is used to set the fractures to be randomly distributed in the reservoir (i.e.,

random fracture starting point f_{random}). Then, the number of fractures, distribution function, morphological parameters, etc., are input into the DFN generation program, so as to obtain the cumulative number set C under the established fracture characteristic parameters. By the obtained growth vector set and accumulated number set, a certain number and range of ordered rough fracture point sets are finally output, thus generating the R-DFN model. And by finding the starting and ending points corresponding to the fractures from the output rough fracture point set, the same number and range of ordered conventional fracture point sets can be output, thus generating the C-DFN model corresponding to the aforementioned R-DFN model.

Numerical model setup

The gas flow in the real reservoir is very complex, and considering the limitations of the simulation conditions, the following assumptions are made:

- (1) The gas is a single-phase flow.
- (2) The saturated Darcy's law of seepage is followed.
- (3) The gas flow is steady-state and isothermal.
- (4) The volume change of the fracture is not considered and the effect of convection flow is neglected.

Then, the continuity equation (Shi et al. 2022) of the gas flow can be expressed as

$$\left\{ \begin{array}{l} \Delta \cdot (\rho_g V) = 0 \\ V = -K \Delta P / \mu \end{array} \right\}, \quad (7)$$

where ρ_g is the gas density, V is the gas flow rate, K is the total permeability of the fractured rocks, μ is the gas viscosity, and ΔP is the pressure gradient. And the total permeability K of the fractured rocks can be expressed as (Luo et al. 2021)

$$K = K_f (1 - \zeta_{\text{im}}(x, y)) + K_p \zeta_{\text{im}}(x, y), \quad (8)$$

where K_f is the fracture network permeability; K_p is the matrix permeability; and $\zeta_{\text{im}}(x, y)$ is the model matrix image function value.

The fracture distribution in fractured rocks usually follows the fractal theory and topological structure distribution pattern. Meanwhile, in the real fracture network, the fractures also have significant tortuous characteristics, i.e., the actual reservoir fractures are rough fractures (Shi et al. 2022). Therefore, permeability estimation considering the connectivity of complex fracture networks is a challenging task. In a previous study, we proposed a fractal permeability model for

rough fracture networks that integrates fracture network geometric parameters, fluid flow patterns and topological connectivity (Eq. (9)), and verified the reasonableness and validity of the model (Shi et al. 2023).

$$K_{\text{fR}} = \frac{(\beta\tau)^{D_{\text{TF}}}(1 - \sin^2\theta)\phi L_0}{12} \left\{ \frac{\beta l_{\text{bmax}}(2 - D_f)(c + 1)}{(3 - D_f) \left[1 - \left(\frac{l_{\text{bmin}}}{l_{\text{bmax}}} \right)^{2-D_f} \right]} + 6\lambda \right\}, \quad (9)$$

where β is the aperture proportionality coefficient, c is the topological connectivity, ϕ is the porosity, L_0 is the characteristic length, λ is the gas molecular free range, τ is the tortuosity, θ is the fracture dip angle, D_{TF} is the tortuosity fractal dimension, D_f is the fractal dimension of the fracture network, l_{bmin} is the minimum branching length, and l_{bmax} is the maximum branching length.

When the values of fracture tortuosity and tortuosity fractal dimension are taken as 1, it is a parallel panel model, assuming that the fractures are smooth straight lines or flat panels. That is, Eq. (9) can be translated into the conventional flat panel fracture network permeability Eq. (10).

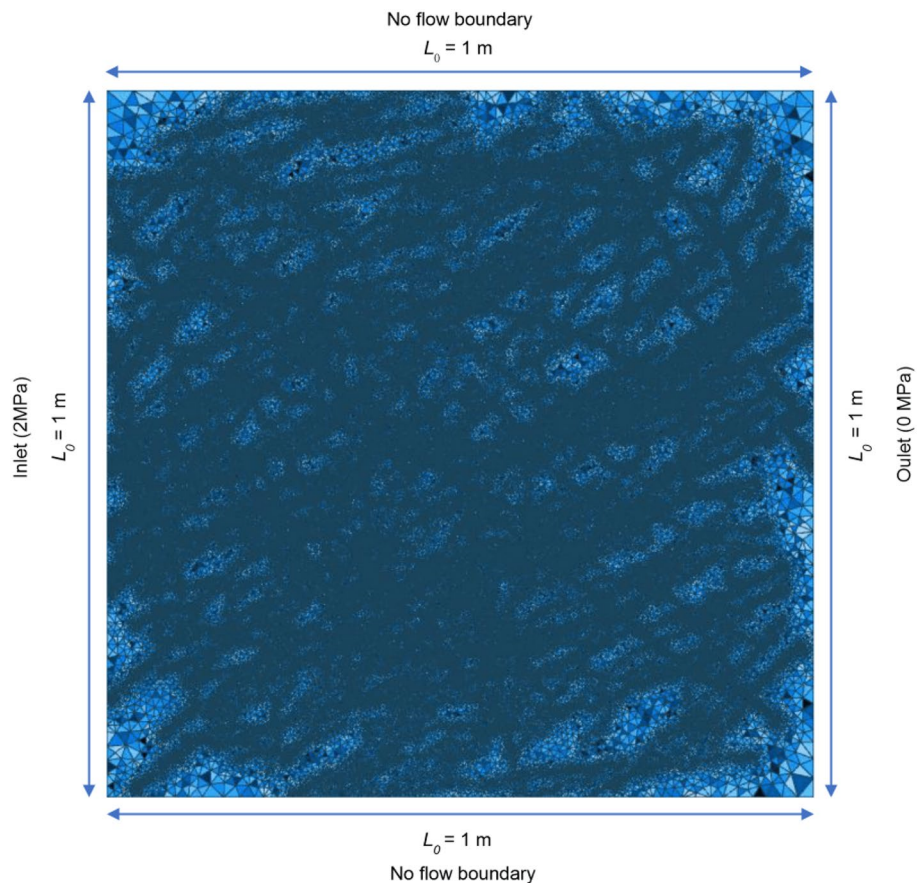
$$K_{\text{fC}} = \frac{\beta(1 - \sin^2\theta)\phi L_0}{12} \left\{ \frac{\beta l_{\text{bmax}}(2 - D_f)(c + 1)}{(3 - D_f) \left[1 - \left(\frac{l_{\text{bmin}}}{l_{\text{bmax}}} \right)^{2-D_f} \right]} + 6\lambda \right\}, \quad (10)$$

The boundary conditions of the simulation are set as shown in Fig. 3. The left boundary of the fractured rock is the gas inlet with pressure $P_1 = 2$ MPa and the right boundary is the gas outlet with pressure $P_2 = 0$ MPa. The pressure gradient from the inlet to the outlet is kept constant and the gas is driven by the pressure. The upper and lower boundaries of the model are no-flow boundaries, i.e., no gas flow. The fractured rock size $L_0 = 1$ m, matrix permeability $K_p = 0.02$ mD. The simulation sets the flowing gas in the fractured rock as CH_4 , and then, the gas viscosity $\mu = 1.1067\text{E} - 5$ Pa*s, gas density $\rho_g = 0.648$ kg/m³, and gas molecular free range $\lambda = 2.815 \times 10^{-9}$ m.

Simulation results comparison

Existing studies (Huang et al. 2021; Yang et al. 2023) show that the statistical law of reservoir fractures conforms to the length power-law distribution (the range of exponent

Fig. 3 Schematic diagram of the boundary conditions



is 1.3–3.5 (Bonnet et al. 2001)) and the angular Fisher distribution. Therefore, referring to the related studies of DFN (Hyman et al. 2015; Luo et al. 2021), the DFN model in this paper adopts the length distribution with power-law exponent of 2.5 and the angle distribution with Fisher coefficient of 6, and includes 300 fractures. Through the modeling method for different DFNs, the DFN model images generated by the program are binarized to build a total of nine groups of fractured rock models with different DFNs, as in Fig. 4, where each group of models includes a fractured rock model with C-DFN and a fractured rock model with R-DFN. For example, C1 and R1 are a group of fractured rock models, C2 and R2 are a group of fractured rock models and so on. In addition, according to the existing fractal permeability studies of fractured rocks (Luo et al. 2021; Klimczak et al. 2010), the fracture aperture proportionality coefficient β is taken in the range of 0.001–0.1. Therefore, the intermediate value of β is taken as 0.03 in this paper. Due to randomness, the generated DFN models have different network structures, i.e., the structural parameters of each group of DFNs are different. For example, the connectivity

of C1–C9 is 2.832, 2.325, 2.468, 3.175, 2.22, 3.792, 2.644, 3.575 and 3.363, respectively; and the connectivity of R1–R9 is 3.439, 3.039, 3.108, 3.591, 2.891, 4.035, 3.222, 3.859 and 3.736, respectively. The other geometric parameters of fractured rocks are shown in Table 1.

The established fractured rock model and Eqs. (8), (9) and (10) were implanted into COMSOL, and the simulation conditions and parameters were used for numerical simulation to obtain the simulation results of fractured rock permeability for different DFNs, as shown in Fig. 5a. The results show that with the increase in connectivity, the fractured rocks with different DFNs all have gradually increased in permeability, and the connectivity and permeability of the fractured rocks with R-DFN are significantly higher than those with C-DFN. The connectivity differences demonstrated in Fig. 5b indicate that there are more Y-type nodes and X-type nodes in R-DFN. According to the topology theory, these two types of nodes are formed by the interconnection or crossover between the fractures. This indicates more frequent connectivity between fractures and higher

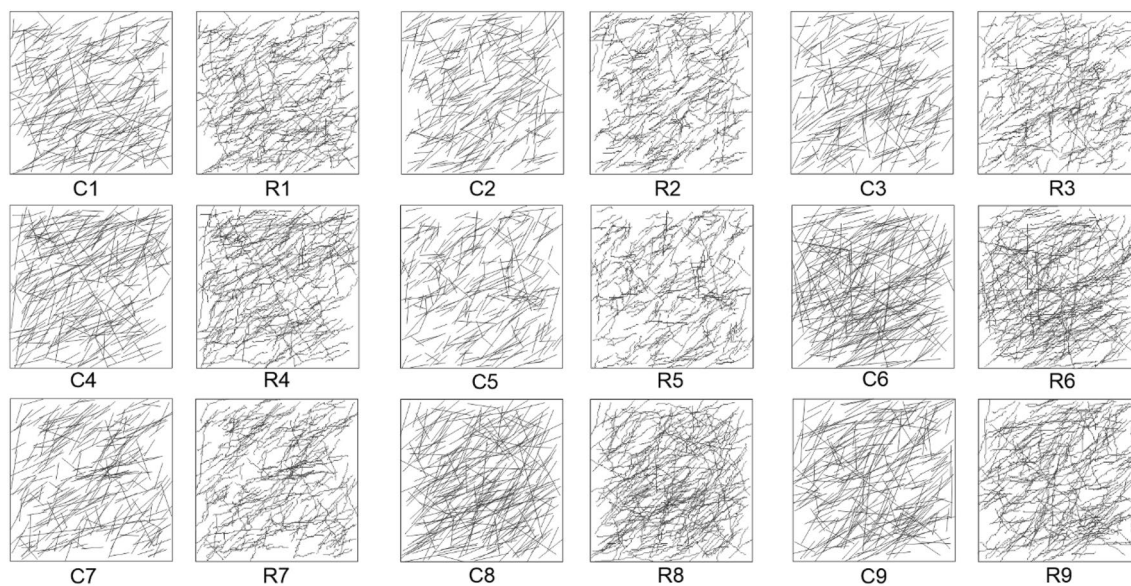
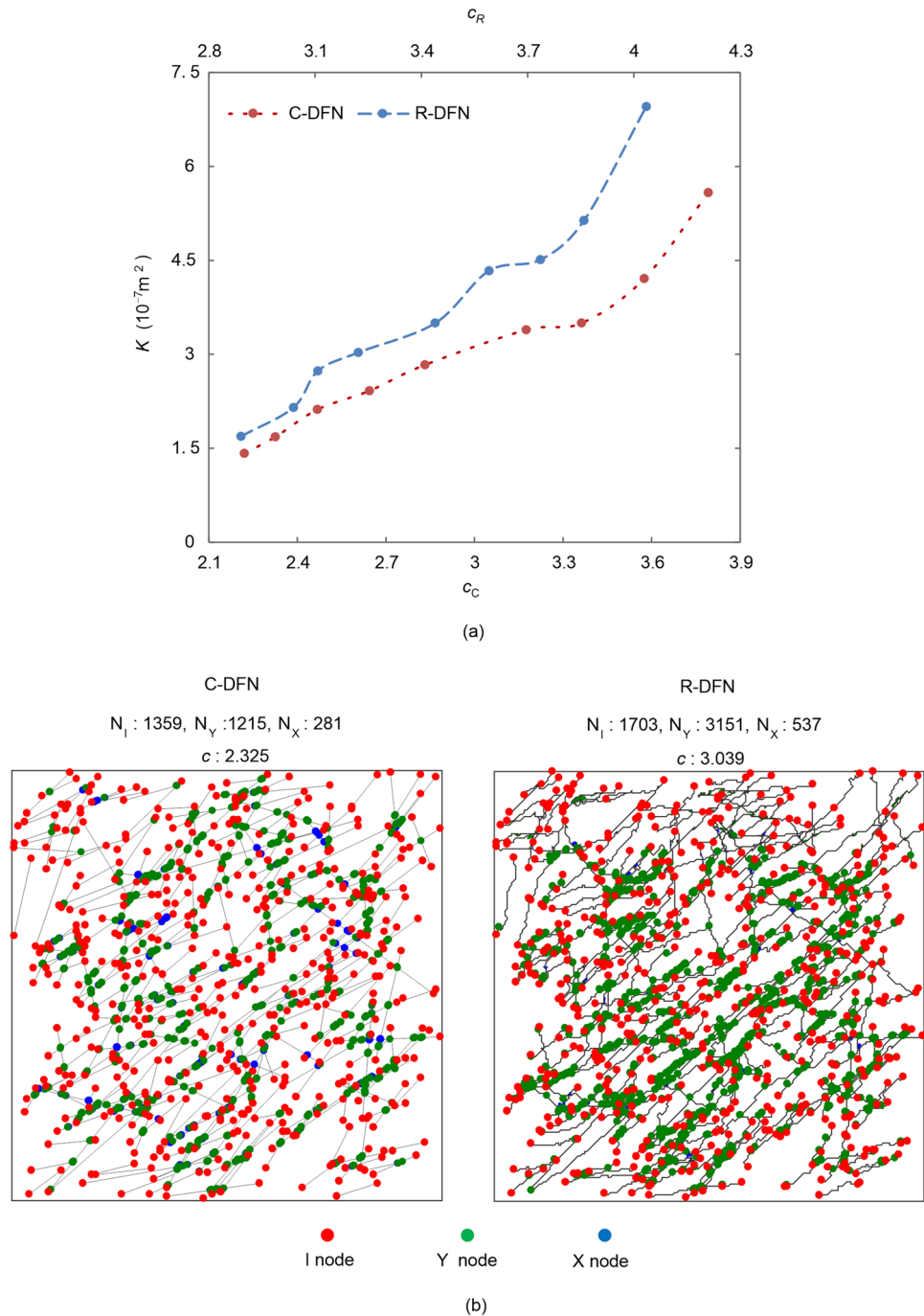


Fig. 4 Fractured rock models: C-DFN and R-DFN

Table 1 Geometric parameters of fractured rock models

Property	D_f	ϕ	τ	D_{Tf}
C1–C9	1.936–1.963	0.131–0.224	1	1
R1–R9	1.940–1.965	0.152–0.245	1.169–1.267	1.040–1.077
Property	l_{bmax}/m	l_{bmin}/m	c	θ
C1–C9	0.262–0.448	0.032–0.042	2.220–3.792	47.4°–52.1°
R1–R9	0.264–0.362	0.032–0.045	2.891–4.035	

Fig. 5 **a** fractured rock permeability (the subscripts *C* and *R* denote C-DFN and R-DFN, respectively) and **b** fracture network connectivity of C-DFN and R-DFN (N_I is the number of the *I*-nodes, N_Y is the number of the *Y*-nodes, and N_X is the number of the *X*-nodes)



connectivity in R-DFN. Therefore, not considering the roughness of the fractures, i.e., using the C-DFN equivalent fracture network in the fractured rock, may underestimate the connectivity of the fracture network. In the same group of fractured rocks, the fracture angle and length distribution of C-DFN and R-DFN are the same, the difference is the fracture roughness of R-DFN. The rough fractures in turn improve the connectivity of the fracture network. And the results show that the fractured rock with R-DFN has higher permeability than the fractured rock

with C-DFN. This phenomenon implies that the inhibiting effect of roughness on gas flow is less than the promoting effect of connectivity on the gas flow. In addition, the difference in fractured rock permeability under the influence of C-DFN and R-DFN increases gradually with the increase in connectivity. Therefore, the simulation results of the two groups of fractured rocks with the smallest difference in permeability (C5 and R5) and the largest difference (C6 and R6) selected from Fig. 5a are shown in Fig. 6.

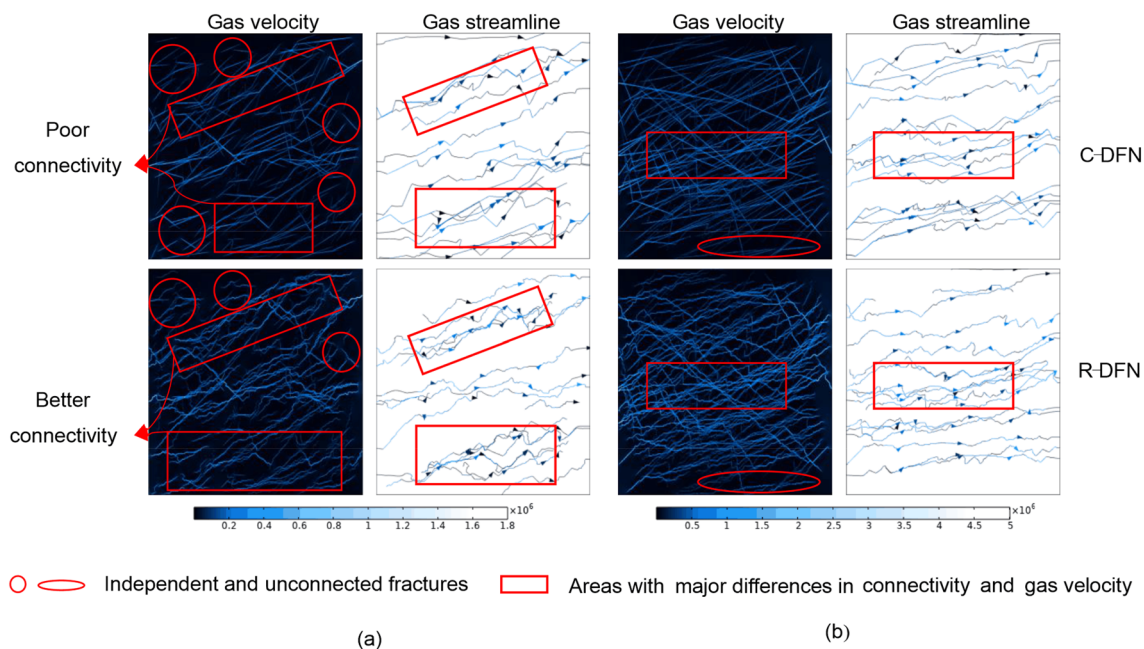


Fig. 6 Comparison of simulation results of fractured rock with different DFNs: **a** C5 and R5, **b** C6 and R6

Figure 6a shows the gas velocity and streamlines of fractured rocks C5 and R5 in Fig. 4, respectively. The simulation results show that the gas velocity cloud of the fractured rock with C-DFN has a slightly darker color and a slightly sparse and more uniform distribution of streamlines. This suggests that the gas velocity of the fractured rock with C-DFN is lower and the difference in gas flow rate within the rock is not significant. A careful comparison of the gas velocity clouds shows that a large number of independent or unconnected fractures (red hollow circles) exist in the fractured rock with C-DFN, while tortuous fractures connect some of the unconnected or independent fractures (red rectangular boxes) in the fractured rock with R-DFN. As a result, the color of the cloud diagram at these locations in the fractured rock with R-DFN is brighter than that of the fractured rock with C-DFN, i.e., the gas velocity is higher. In addition, the streamlines of fractured rock with R-DFN are dense (red rectangular box) at the above position of the streamline diagram. And the density of streamlines also reflects the magnitude of the flow rate. Therefore, it can be concluded that the fractured rocks with R-DFN have a higher degree of inter-fracture connectivity (i.e., better connectivity) and higher gas velocity and permeability. However, although the roughness of R-DFN connects part of the fractures, there are still quite a number of independent fractures (red hollow circles) in Fig. 6a. And these fractures contribute little to the seepage of the fractured rock and even weaken the seepage capacity of the fractured rock.

Therefore, the difference in connectivity of this group of fractured rocks shown in Fig. 6a is more obvious, while the difference in permeability is smaller.

Figure 6b shows the gas velocity and streamlines of fractured rocks C6 and R6 in Fig. 4, respectively. Similar to Fig. 6a, the gas velocity cloud diagram of the fractured rock with R-DFN in Fig. 6b has a brighter color, i.e., the gas velocity is higher. However, it is different from Fig. 6a that the area of the brightly colored gas velocity cloud is larger, i.e., the gas velocity is generally higher in the fractured rock with R-DFN. Especially, in the middle of the fractured rock body (red rectangular box), it can be observed that the fracture network in the fractured rock with R-DFN is more complicated due to the tortuous characteristic of fractures. It is easy to form wider flow channels when multiple fractures are connected to each other, i.e., the area of gas flow channels is increased. Therefore, the gas will flow more easily in the middle of the fractured rock R6. It can also be seen from the streamline diagram in Fig. 6b that the streamlines are densest in the middle of the fractured rock R6 compared to the fractured rock C6 (red rectangular box), i.e., the gas velocity is highest in the middle of the fractured rock R6. Therefore, even though a small number of unconnected fractures (red ellipses) exist in the fractured rock R6, the fractured rock R6 still has a high permeability due to the high connectivity of its fracture network. Comparing Figs. 6a and b, it can be found that the fractured rocks in Fig. 6a have a large number of independent fractures and unconnected fractures, and the connectivity of their fracture networks is low. The difference in permeability between fractured rocks C6 and R6 is also small. In contrast,

the fractured rocks C5 and R5 in Fig. 6b are the opposite. Therefore, it can be inferred that independent fractures, unconnected fractures and fracture network connectivity significantly affect the differences in the permeability assessment of fractured rocks.

Influence of different parameters on the permeability of fractured rocks under different DFNs

Connectivity, porosity, maximum branch length and fracture angle are model parameters common to both C-DFN and R-DFN. However, the results of permeability assessment under the influence of the above parameters may differ when C-DFN and R-DFN are used for modeling, respectively. Therefore, a comparative study of fractured rock permeability under the influence of different DFN parameters is presented in this section. Considering that the simulation results in previous section contain only nine groups of fractured rock models, this section adopts the aforementioned reconstruction method and the simulation settings to supplement the simulation results of multiple groups of fractured rock permeability to improve the reliability of the results (the geometric parameters are shown in Table 2). This section compares the effects of the connectivity of different DFNs on the assessment results of fractured rock permeability, firstly. Then, the simulation results are used to compare the effects of the porosity of different DFNs on the assessment results of fractured rock permeability. Finally, this section compares the effects of maximum branch length and fracture dip angle of different DFNs on the assessment results of fractured rock permeability, respectively.

Connectivity

Connectivity reflects the degree of connectivity between fractures in a fracture network (Sanderson and Nixon 2018). The simulation results in the previous section show that the connectivity has a significant effect on the gas flow rate

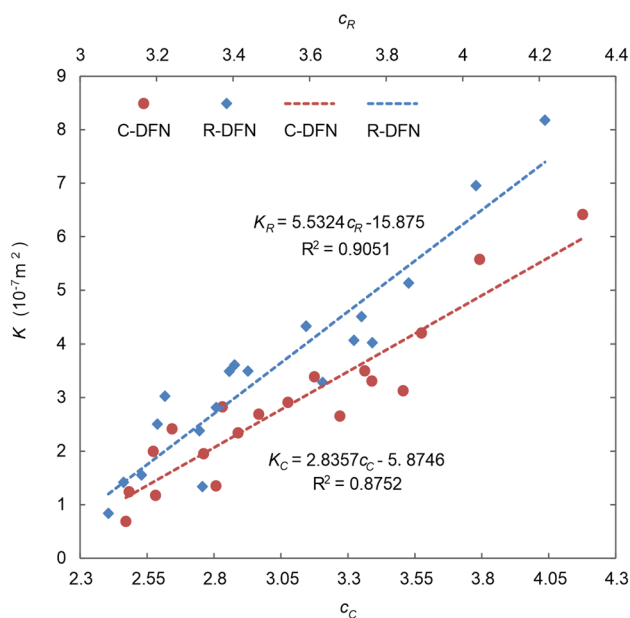


Fig. 7 Relationship between connectivity and permeability of fractured rocks with different DFNs

and permeability of the fractured rocks. The relationship between connectivity and permeability of fractured rocks with different DFNs is shown in Fig. 7. The results show that the fractured rock permeability increases with the growth of connectivity regardless of whether the R-DFN model or the C-DFN model is used. The permeability and connectivity are significantly positively correlated with a linear fit, which is consistent with the relationship between connectivity and permeability in Eqs.(9)(8) and (10)(9). This indicates that connectivity has a non-negligible effect on the permeability of fractured rocks with complex fracture networks. The increase in connectivity indicates that the connection, intersection and overlap between fractures increase, which provides more convenient channels for gas flow and makes it easier for gas to flow toward the outlet of the fractured rocks, thus increasing the gas flow rate and enhancing the fractured rock permeability (Xu et al. 2006). From the fitting results, it can be seen that the slope of the fitting function of the permeability of the fractured rocks with R-DFN is larger.

Table 2 Geometric parameters of fractured rocks ($\beta=0.03$)

Property	D_f	ϕ	τ	D_{Tf}
C-DFN	1.810–1.969	0.071–0.230	1	1
R-DFN	1.810–1.971	0.079–0.250	1.133–1.267	1.030–1.077
Property	l_{bmax}/m	l_{bmin}/m	c	θ
C-DFN	0.237–0.524	0.029–0.060	2.471–4.177	46.4°–69.3°
R-DFN	0.245–0.415	0.029–0.063	3.074–4.215	

With the growth of connectivity, the growth of permeability of fractured rocks with R-DFN is more significant than the growth of permeability of fractured rocks with C-DFN. This suggests that the permeability of fractured rocks with R-DFN is more sensitive to the change of connectivity. For the fractured rocks with high connectivity, using the C-DFN model to evaluate the fractured rock permeability will make the evaluation result low.

The gas velocity clouds of the fractured rocks corresponding to the minimum ($c_{Cmin} = 2.471$, $c_{Rmin} = 3.074$) and maximum ($c_{Cmax} = 4.177$, $c_{Rmax} = 4.215$) values of connectivity in Fig. 7 are selected and displayed in Fig. 8, respectively. It can be clearly seen that the gas velocity clouds of the fractured rocks with the highest connectivity are very bright and have the highest flow velocities at the gas inlet

and outlet compared to the fractured rocks with the lowest connectivity. The conventional and rough fracture networks with the highest connectivity are dense, and their fractures cross, connect and overlap each other more frequently, so their fracture networks have higher connectivity. In the fracture network with the lowest connectivity, although there is some crossover between fractures, there are still more unconnected fractures, so there are fewer flow channels connecting the entrance to the exit, which reduces the gas flow velocity, and therefore the corresponding gas velocity cloud map of the fractured rock is darker. This indicates that the connectivity between fractures will significantly increase the fluid velocity and promote gas flow, thus improving the fractured rock permeability. Therefore, enhancing fracture network connectivity by modifying reservoir fractures can

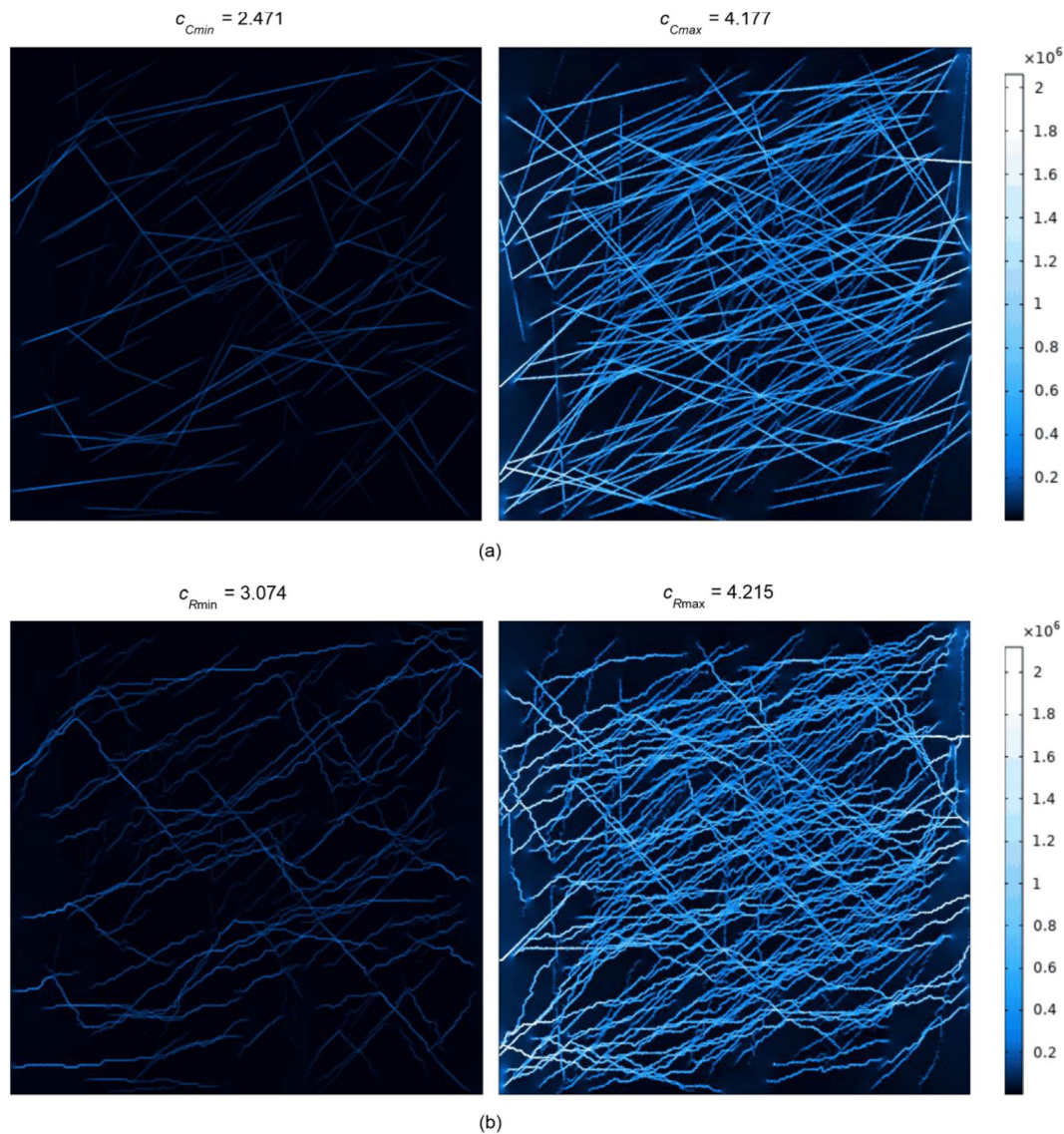


Fig. 8 Gas velocity clouds of fractured rocks with different connectivities: **a** C-DFN, **b** R-DFN

effectively promote reservoir gas flow and improve reservoir permeability, thereby contributing to reservoir development and production capacity enhancement.

In addition, similar to the simulation results in the previous section, the differences in permeability and gas velocity of fractured rocks with different DFNs are larger when the connectivity is higher, while the opposite is true when the connectivity is lower. And based on the fitting function in Fig. 7, it can be inferred that when the connectivity is smaller, the permeability of fractured rocks with different DFNs in the same group may be the same, and even the permeability assessment result of fractured rocks with C-DFN will be higher than that of fractured rocks with R-DFN. This may be due to the fact that the smaller the connectivity, the more independent and unconnected fractures in the fractured rocks. This can be observed in both Fig. 6 and Fig. 8. At this time, the hindering effect of rough fractures on gas flow is more obvious than the promoting effect of connectivity on the gas flow. Therefore, the permeability of the fractured rock with R-DFN will become lower and lower, even lower than that of the fractured rock with C-DFN. This is also the reason why the permeability of fractured rocks with rough fractures is lower in most studies of single fractures. It can be concluded that when the fracture network in the fractured rocks is complex and dense, the role of connectivity in promoting gas flow is dominant. In contrast, when the fracture network in the fractured rocks is simple and sparse, or when the fractured rocks are single-fractured, the role of fracture roughness in hindering gas flow is dominant.

Porosity

Porosity refers to the ratio of the volume of channels allowed for fluid flow within the rock mass to the volume of the rock mass, and reflects the proportion of seepage channels in the rock mass (Luo et al. 2021). Therefore, porosity has been of interest to researchers as an important parameter for assessing the permeability of rock masses (Sheng et al. 2019). In this section, we show the simulation results of permeability of conventional and rough fractured rocks in Fig. 9 in order to specifically analyze the relationship between porosity and permeability under different DFNs. The results show that the permeability of both fractured rocks with R-DFN and those with C-DFN increases with increase in porosity in a polynomial fit. This is consistent with the regularity shown in the past study (Shi et al. 2022). The increase in porosity indicates that the fracture network provides more flow channels for the gas, resulting in increased gas flow in the fractured rock at the same time (Li et al. 2016). Therefore, the gas flow rate increases and the fractured rock permeability is enhanced. In addition, it can be observed that the difference in permeability between

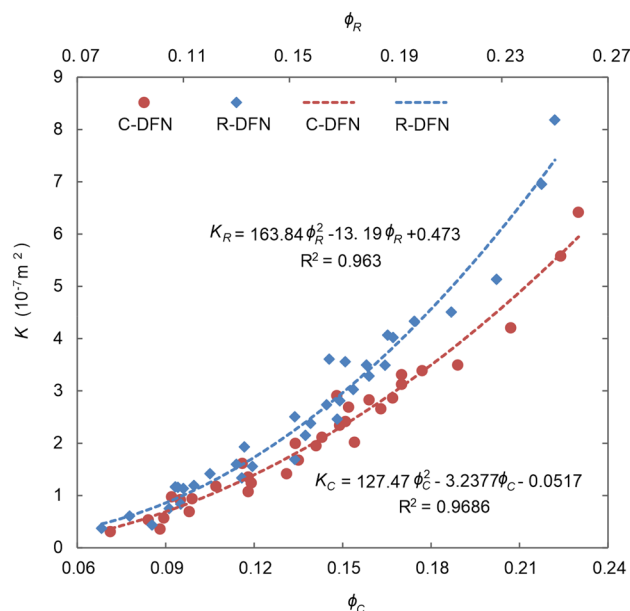


Fig. 9 Relationship between permeability and porosity of fractured rocks with different DFNs

fractured rocks with R-DFN and fractured rocks with C-DFN increases with increase in porosity. This may be due to the more adequate connection between the rough fractures, while the interconnection between the rough fractures produces a larger area of dominant flow channels. With the increase in porosity, the gas dominant flow channels in the fractured rocks with R-DFN also gradually increase. As a result, the difference in permeability of fractured rocks with the different DFNs also gradually increases. Analyzing the result data, it can be found that the porosity of the fractured rocks with C-DFN and the fractured rocks with R-DFN increased by 2.24 times and 2.16 times, respectively, while the permeability of both increased by approximately 20 times and 21 times, respectively. Therefore, it can be believed that the permeability of fractured rocks using the R-DFN model is more sensitive to porosity. When the fractured rocks have high porosity, using C-DFN to evaluate the permeability of the fractured rocks can underestimate the actual permeability of the fractured rocks more obviously.

The gas velocity clouds of the fractured rocks corresponding to the minimum ($\phi_{Cmin} = 0.071$, $\phi_{Rmin} = 0.079$) and maximum ($\phi_{Cmax} = 0.23$, $\phi_{Rmax} = 0.25$) values of porosity in Fig. 9 are extracted, as in Fig. 10. The simulation results show that the gas flow rate of the fractured rock with the largest porosity is significantly larger than that of the fractured rock with the smallest porosity, and the difference between them is one order of magnitude. The fracture network with fewer fractures and less complexity has smaller porosity and lower gas flow rate. The smaller the porosity of the rock, the fewer channels are

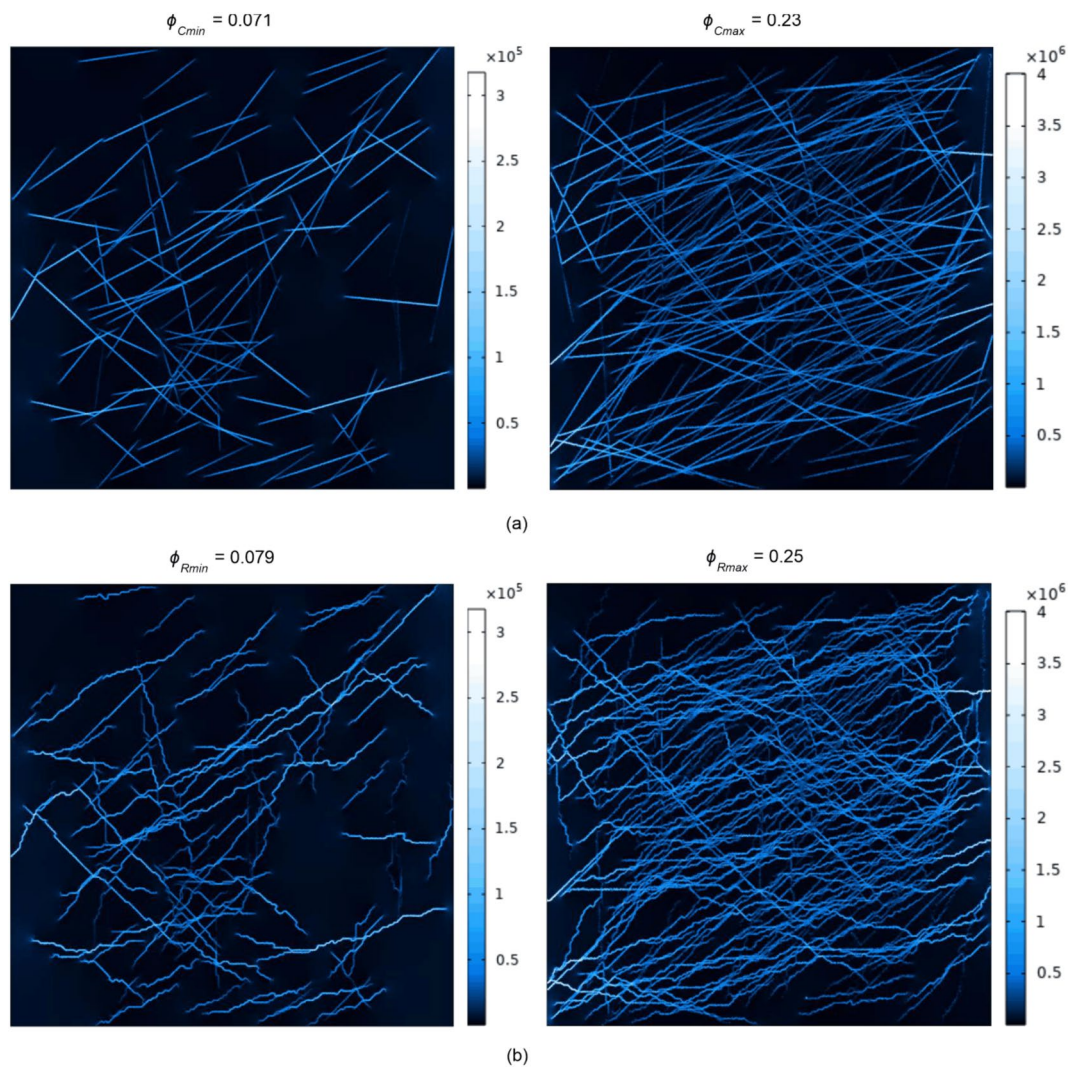


Fig. 10 Simulation results of fractured rocks with different porosity: **a** C-DFN, **b** R-DFN

provided for gas flow, and the smaller the possibility of interconnection between fractures. As a result, the narrower the dominant gas flow channel formed, the more the gas flow is limited. Therefore, the slower the gas flow rate, the lower the permeability of the corresponding fractured rocks. In addition, the morphological structure and porosity of the fracture network in the fractured rocks corresponding to the minimum and maximum porosity are significantly different. In addition, there are a large number of independent fractures and unconnected fractures in the fractured rocks with minimum porosity. Thus, the gas velocity and permeability of their corresponding fractured rocks are lower.

Maximum branch length

The fracture length controls the length of the main seepage channel in fractured rocks. Studies have shown that the

longer the fracture length, the higher the permeability and the better the seepage capacity of the fractured rocks (Zhu and Cheng 2018). However, the fracture length in the fracture network has a large uncertainty, while this uncertainty can be avoided by using fracture branch length. The relationship between permeability and maximum branch length of fractured rocks with different DFNs is shown in Fig. 11. The results show that the longer the maximum branch length, the lower the fractured rock permeability. The maximum branch length of the fracture network reflects the level of connectivity of the network to a certain extent (Lahiri 2021). When the fracture length is constant, the longer the maximum branch length indicates that there are fewer nodes dividing the fracture, and the connectivity of the fracture network is smaller (Loza Espejel et al. 2020). According to the results in Section connectivity, the smaller the connectivity of the fracture network, the lower the

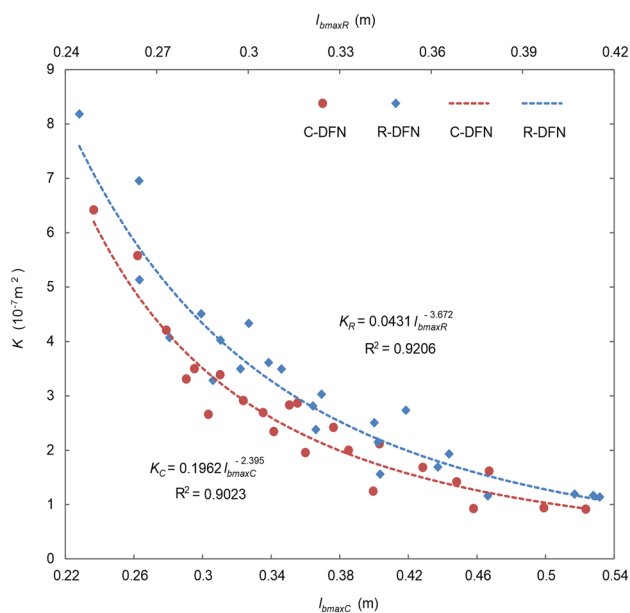


Fig. 11 Relationship between permeability and maximum branch length of fractured rocks with different DFNs

permeability of the fractured rocks. That is, the longer the maximum branch length, the lower the fractured rock permeability. The simulation results of fractured rocks with different DFNs in Fig. 11 also corroborate the above inference. Further analysis of the results data shows that the maximum branch length of the fractured rocks with C-DFN increases by 121% and the permeability decreases by 86%, while the maximum branch length of the fractured rocks with R-DFN increases by 69% and the permeability decreases by 86%. In addition, the fitted curves show that the decrease in permeability is gradually slow with the increase in the maximum branch length. This means that the smaller the maximum branch length, the more obvious the effect on the permeability of the fractured rocks. In other words, for fractured rocks with a high connectivity degree, the maximum branch length has a significant effect on the permeability. Therefore, it can be believed that the permeability of fractured rocks with R-DFN is more sensitive to the change of maximum branch length. On the other hand, it also implies that the permeability of fractured rocks with R-DFN is also more sensitive to the connectivity, which is consistent with the conclusion in Section connectivity.

Fracture dip angle

To analyze the effect of fracture dip angle (the angle between the gas flow direction and the fracture) on the fractured rock permeability, we extracted the average fracture dip angle (45° – 70°) and its corresponding fractured rock permeability

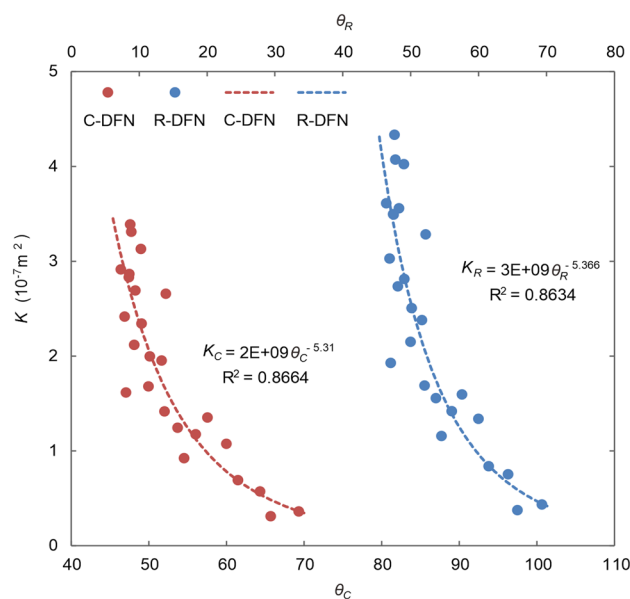


Fig. 12 Relationship between permeability and fracture dip of fractured rocks with different DFNs

for multiple groups of fracture networks. Figure 12 shows the relationship between the average fracture dip angle and the fractured rock permeability. The results show that the effect of fracture dip angle on the fractured rock permeability is significant. This is because gas flows mainly in the fracture network, and the fluid resistance flowing through the fractures increases with the increase in fracture dip angle (Xia et al. 2021; Liu et al. 2021). Therefore, the fractured rock permeability decreases with the increase in fracture angle. In each group of fractured rocks, each conventional linear fracture of C-DFN is determined by the starting and ending points of its corresponding rough fracture in R-DFN. Therefore, the dip angle and distribution of fractures in the same group of fractured rocks with C-DFN and those with R-DFN are the consistent, which can also be clearly observed from Fig. 4. Therefore, the average fracture dip angles of fractured rocks with different DFNs in the same group are also the equal. The result data show that the permeability of the fractured rocks with R-DFN (about $4.5 \times 10^{-7} \text{ m}^2$) is larger than that of the fractured rocks with C-DFN (about $3.5 \times 10^{-7} \text{ m}^2$) when the fracture dip angle is around 45° . However, the permeability of both decreases to about $0.5 \times 10^{-7} \text{ m}^2$ at the same time when the fracture dip angle is around 70° . Therefore, it can be believed that the permeability of the fractured rocks with R-DFN is more sensitive to the change of fracture dip angle. This may be because the increase in fracture dip angle enhances the degree of resistance to fluid flow by the tortuosity of the rough fracture, which makes the gas flow more slowly and thus reduces the fractured rock permeability more greatly.

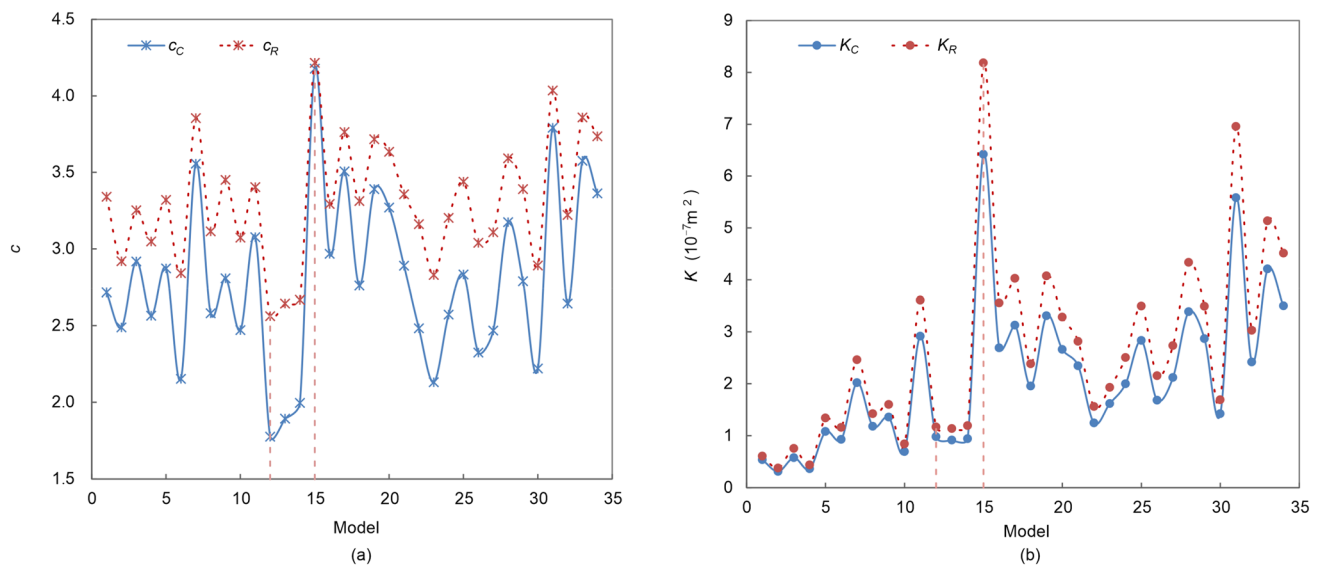


Fig. 13 **a** fracture network connectivity and **b** permeability of fractured rocks with different DFNs

Discussion

The simulation results of the fractured rocks in previous chapter are extracted and their fracture network connectivity is shown in Fig. 13a and the corresponding permeability is shown in Fig. 13b. The results show that the fracture network connectivity and permeability of the fractured rocks with R-DFN are higher. The tortuous characteristics of rough fractures increase the crossings, overlaps and connections between fractures, thus improving the connectivity of the fracture network, and thus the connectivity of R-DFN will be better than that of C-DFN. The results in section connectivity show that fracture network connectivity has a significant positive correlation with the permeability of fractured rocks, and the permeability increases with the increase in connectivity. In previous studies (Xia et al. 2021; Shi et al. 2022), the tortuosity (roughness) of rough fractures has an inhibiting effect on the gas flow in the fracture network, which decreases the fractured rocks permeability and thus weakens its seepage capacity. And the results in Fig. 13 show that the permeability of the fractured rocks with R-DFN which has higher connectivity will be greater than that of the fractured rocks with C-DFN. Therefore, for the permeability of fractured rocks with complex fracture networks, the promoting effect of fracture network connectivity is greater than the hindering effect of rough fracture tortuosity, i.e., the contribution of connectivity to the fractured rock permeability is dominant. Comparing the fracture network connectivity and permeability of the fractured rocks in each group, it can be found that the fracture network connectivity of the fractured rocks in the

12th group model differs greatly, but their corresponding fractured rock permeability is very similar. In contrast, the fracture network connectivity of fractured rocks in the 15th group model is very close, but their corresponding fractured rock permeability has a significant difference. To explore this phenomenon, we extracted the gas velocity clouds of the above two groups of fractured rocks separately, as shown in Fig. 14.

Comparing C-DFN and R-DFN in Fig. 14a, it can be found that the interaction between fractures in R-DFN is more frequent. The originally unconnected straight fractures in C-DFN are interconnected in R-DFN to form through tortuous fractures (red rectangle). Thus, the connectivity of R-DFN is significantly higher than that of C-DFN. However, it can also be observed that there are still a large number of independent fractures and unconnected fractures in the C-DFN and R-DFN of Fig. 14a. These fractures significantly decrease the permeability of the fractured rocks. Therefore, the difference in permeability between the two fractured rocks is small, even though the straight fractures and rough fractures form the two DFNs with very different connectivities, respectively. Comparing the C-DFN and R-DFN in Fig. 14b, it is observed that both fracture networks are very dense and complex, and the degree of connectivity is significantly higher than that in Fig. 14a. Since the rough fractures are more easily connected with their surrounding neighboring fractures, there are more connected fractures at the exit boundary of the fractured rock with R-DFN, and thus the gas flow at the exit boundary of the fractured rock with R-DFN will be significantly larger than that of the fractured rock with C-DFN. The gas velocity cloud at the exit boundary of

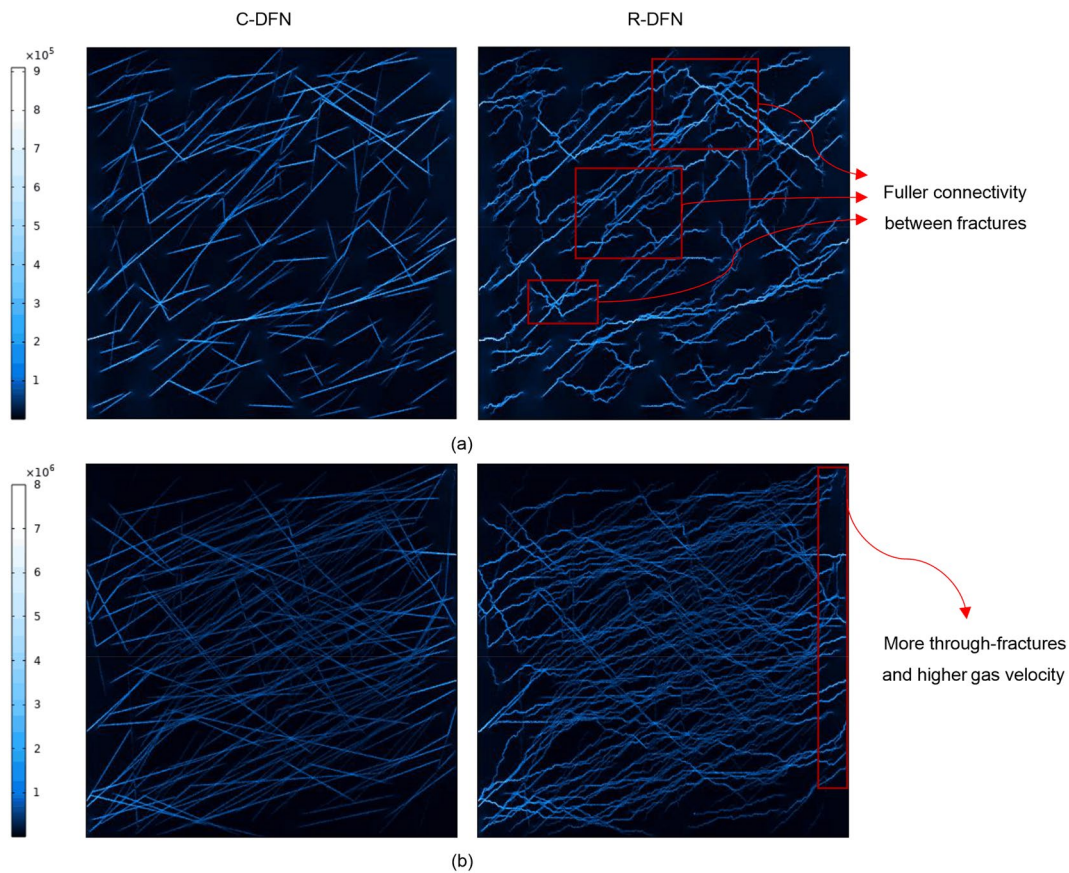


Fig. 14 Simulation results of fractured rocks with different DFNs: **a** Model 12, **b** Model 15

the fractured rock with R-DFN in Fig. 14b is lighter and brighter (red rectangle), i.e., the gas velocity at the exit of this fractured rock is larger, and thus the permeability of the fractured rock with R-DFN is larger than that of the fractured rock with C-DFN. It is thus clear that the evaluation of fractured rock permeability is a complex problem, where parameters such as exit boundary, connectivity, porosity, branch length and fracture dip angle not only affect each other but also jointly influence the fractured rock permeability.

Conclusions

In this paper, based on the discrete fracture network (DFN) modeling method, the fractured rock models with conventional DFN (C-DFN) and rough DFN (R-DFN) are established. The differences in permeability assessment and parameter sensitivities of fractured rocks resulting from the fracture network characterization using C-DFN and R-DFN are analyzed by numerical simulation of fractured rock seepage. The differences in fracture network connectivity and permeability of fractured rocks with C-DFN and R-DFN

are discussed. The main conclusions obtained from this study are as follows.

- (1) The unconnected fractures and independent fractures in the fracture network contribute less to the fractured rock permeability, and even weaken the seepage capacity of the fractured rocks. The fractured rock permeability increases with increase in connectivity and porosity, and decreases with increase in maximum branch length and fracture dip angle.
- (2) Ignoring the roughness of the fractures, i.e., using C-DFN to equivalent the fracture network in the fractured rocks, may underestimate the connectivity of the fracture networks. For the fractured rocks with high fracture network connectivity, using the C-DFN model to assess the fractured rock permeability may underestimate the assessment result. In contrast, when the connectivity is very low, the permeability assessment results of fractured rock with C-DFN may overestimate the fractured rock permeability.
- (3) For the fractured rocks with R-DFN, when the fracture network in the fractured rocks is more complex and denser, the positive influence of connectivity on

gas flow is dominant. In contrast, when the fracture network in the fractured rock is simpler and sparser, or when it is a single-fractured rock, the inhibiting effect of fracture roughness on gas flow is dominant. Compared with the fractured rocks with C-DFN, the permeability of the fractured rocks with R-DFN is more sensitive to the parameters of connectivity, porosity, maximum branch length and fracture dip angle.

- (4) The higher the fracture network connectivity and porosity of the fractured rocks, the faster the gas flow rate in the fractured rocks, and the more obvious the difference in the permeability assessment of the fractured rocks using C-DFN and R-DFN. However, the current study is limited to two-dimensional DFNs, and how to establish three-dimensional DFNs conforming to the actual morphology for fracture networks in three-dimensional space still needs to be further explored.

Funding The authors gratefully acknowledge the financial support given by the National Natural Science Foundation of China (52104046, U22B6003, U22A20166, 52374122 and 51974148), and the Open Research Fund of State Key Laboratory of Geomechanics and Geotechnical Engineering, Institute of Rock and Soil Mechanics, Chinese Academy of Sciences, Grant NO.SKLGME022020.

Data availability The data used to support the findings of this study are available from the corresponding author upon request.

Declarations

Conflict of interest The authors declare that there are no conflicts of interest regarding the publication of this paper.

Open Access This article is licensed under a Creative Commons Attribution 4.0 International License, which permits use, sharing, adaptation, distribution and reproduction in any medium or format, as long as you give appropriate credit to the original author(s) and the source, provide a link to the Creative Commons licence, and indicate if changes were made. The images or other third party material in this article are included in the article's Creative Commons licence, unless indicated otherwise in a credit line to the material. If material is not included in the article's Creative Commons licence and your intended use is not permitted by statutory regulation or exceeds the permitted use, you will need to obtain permission directly from the copyright holder. To view a copy of this licence, visit <http://creativecommons.org/licenses/by/4.0/>.

References

- Abdelazim R (2020) An integrated approach for relative permeability estimation of fractured porous media: laboratory and numerical simulation studies. *J Pet Explor Prod Technol* 10:1–18. <https://doi.org/10.1007/s13202-016-0250-x>
- Abe S, Deckert H (2021) Roughness of fracture surfaces in numerical models and laboratory experiments. *Solid Earth* 12:2407–2424. <https://doi.org/10.5194/se-12-2407-2021>
- Al-Dujaili AN, Shabani M, Al-Jawad MS (2021) Identification of the best correlations of permeability anisotropy for Mishrif reservoir in West Qurna/1 oil Field Southern Iraq. *Egypt J Pet* 30:27–33. <https://doi.org/10.1016/j.ejpe.2021.06.001>
- Barton N (1973) Review of a new shear-strength criterion for rock joints. *Eng Geol* 7:287–332. [https://doi.org/10.1016/0013-7952\(73\)90013-6](https://doi.org/10.1016/0013-7952(73)90013-6)
- Bonnet E, Bour O, Odling NE, Davy P, Main I, Cowie P, Berkowitz B (2001) Scaling of fracture systems in geological media. *Rev Geophys* 39:347–383. <https://doi.org/10.1029/1999RG000074>
- Daghighi H, Tannant DD, Daghighi V, Lichti DD, Lindenberg R (2022) A critical review of discontinuity plane extraction from 3D point cloud data of rock mass surfaces. *Comput Geosci* 169:105241. <https://doi.org/10.1016/j.cageo.2022.105241>
- Dong Y, Yunmei Fu, Yeh T-C, Wang Y-L, Zha Y, Wang L, Hao Y (2019) Equivalence of discrete fracture network and porous media models by hydraulic tomography. *Water Resour Res* 55:3234–3247. <https://doi.org/10.1029/2018WR024290>
- Fang T, Feng Q, Zhou R, Guo C, Wang S, Gao K (2023) A coupled thermal–hydrological–mechanical model for geothermal energy extraction in fractured reservoirs. *J Pet Explor Prod Technol* 13:2315–2327. <https://doi.org/10.1007/s13202-023-01665-8>
- Espejel RL, Alves TM, Blenkinsop TG (2020) Multi-scale fracture network characterisation on carbonate platforms. *J Struct Geol* 140:104160. <https://doi.org/10.1016/j.jsg.2020.104160>
- Gao Qi, Han S, Cheng Y, Li Y, Yan C, Han Z (2021) Apparent permeability model for gas transport through micropores and microfractures in shale reservoirs. *Fuel* 285:119086. <https://doi.org/10.1016/j.fuel.2020.119086>
- Hosseini E, Sarmadivaleh M, Chen Z (2021) Developing a new algorithm for numerical modeling of discrete fracture network (DFN) for anisotropic rock and percolation properties. *J Pet Explor Prod* 11:839–856. <https://doi.org/10.1007/s13202-020-01079-w>
- Hosseinzadeh S, Kadkhodaie A, Wood DA, Rezaee R, Kadkhodaie R (2023) Discrete fracture modeling by integrating image logs, seismic attributes, and production data: a case study from Ilam and Sarvak Formations Danan Oilfield, Southwest of Iran. *J Pet Explor Prod Technol* 13:1053–1083. <https://doi.org/10.1007/s13202-022-01586-y>
- Hu M, Rutqvist J (2022) Multi-scale coupled processes modeling of fractures as porous, interfacial and granular systems from rock images with the numerical manifold method. *Rock Mech Rock Eng* 55:3041–3059. <https://doi.org/10.1007/s00603-021-02455-6>
- Huang Na, Liu R, Jiang Y, Cheng Y (2021) Development and application of three-dimensional discrete fracture network modeling approach for fluid flow in fractured rock masses. *J Nat Gas Sci Eng* 91:103957. <https://doi.org/10.1016/j.jngse.2021.103957>
- Hyman JD, Painter SL, Viswanathan H, Makedonska N, Karra S (2015) Influence of injection mode on transport properties in kilometer-scale three-dimensional discrete fracture networks. *Water Resour Res* 51:7289–7308. <https://doi.org/10.1002/2015WR017151>
- Ji L, Fengyang Xu, Lin M, Jiang W, Cao G, Songtao Wu, Jiang X (2023) Rapid evaluation of capillary pressure and relative permeability for oil–water flow in tight sandstone based on a physics-informed neural network. *J Pet Explor Prod Technol*. <https://doi.org/10.1007/s13202-023-01682-7>
- Jia Y, Song C, Liu R (2022) The frictional restrengthening and permeability evolution of slipping shale fractures during seismic cycles. *Rock Mech Rock Eng* 55:1791–1805. <https://doi.org/10.1007/s00603-021-02751-1>
- Khodaei M, Delijani EB, Hajipour M, Karroubi K, Dehghan AE (2021) Analyzing the correlation between stochastic fracture networks geometrical properties and stress variability: a rock and fracture parameters study. *J Pet Explor Prod* 11:685–702. <https://doi.org/10.1007/s13202-020-01076-z>

- Klimczak C, Schultz R, Parashar R, Reeves D (2010) Cubic law with aperture-length correlation: implications for network scale fluid flow. *Hydrogeol J* 18:851–862. <https://doi.org/10.1007/s10040-009-0572-6>
- Lahiri S (2021) Estimating effective permeability using connectivity and branch length distribution of fracture network. *J Struct Geol* 146:104314. <https://doi.org/10.1016/j.jsg.2021.104314>
- Lavrov A (2021) Million node fracture: size matters? *J Pet Explor Prod Technol* 11:4269–4276. <https://doi.org/10.1007/s13202-021-01296-x>
- Li Bo, Liu R, Jiang Y (2016) A multiple fractal model for estimating permeability of dual-porosity media. *J Hydrol* 540:659–669. <https://doi.org/10.1016/j.jhydrol.2016.06.059>
- Li Y, Hou J, Guo X (2019) Three-dimensional structural modeling of a low permeability reservoir in the Banqiao formation of the Maxi Oilfield. *J Pet Explor Prod Technol* 9:1897–1906. <https://doi.org/10.1007/s13202-019-0616-y>
- Li X, Li D, Yi Xu, Feng X (2020) A DFN based 3D numerical approach for modeling coupled groundwater flow and solute transport in fractured rock mass. *Int J Heat Mass Transf* 149:119179. <https://doi.org/10.1016/j.ijheatmasstransfer.2019.119179>
- Lin Y, Liu S, Gao S, Yuan Y, Wang J, Xia S (2021) Study on the optimal design of volume fracturing for shale gas based on evaluating the fracturing effect—a case study on the Zhao Tong shale gas demonstration zone in Sichuan China. *J Pet Explor Prod* 11:1705–1714. <https://doi.org/10.1007/s13202-021-01134-0>
- Liu X, Jin Y, Lin B, Zhang Q, Wei S (2021) An integrated 3D fracture network reconstruction method based on microseismic events. *J Nat Gas Sci Eng* 95:104182. <https://doi.org/10.1016/j.jngse.2021.104182>
- Lu C, Liu J, Huang F, Wang J, Zhou G, Wang J, Meng X, Liu Y, Wang X, Shan X, Liang H, Guo J (2022) Numerical simulation of proppant embedment in rough surfaces based on full reverse reconstruction. *J Pet Explor Prod Technol* 12:2599–2608. <https://doi.org/10.1007/s13202-022-01512-2>
- Luo Y, Xia B, Li H, Huarui Hu, Mingyang Wu, Ji K (2021) Fractal permeability model for dual-porosity media embedded with natural tortuous fractures. *Fuel* 295:120610. <https://doi.org/10.1016/j.fuel.2021.120610>
- Luo X, Cheng Y, Tan C (2023) Calculation method of equivalent permeability of dual-porosity media considering fractal characteristics and fracture stress sensitivity. *J Pet Explor Prod Technol* 13:1691–1701. <https://doi.org/10.1007/s13202-023-01640-3>
- Mandelbrot BB (1982) *The fractal geometry of nature*. WH freeman, New York
- Nguyen HT, Lee JH, Elraies KA (2022) Review of pseudo-three-dimensional modeling approaches in hydraulic fracturing. *J Pet Explor Prod Technol* 12:1095–1107. <https://doi.org/10.1007/s13202-021-01373-1>
- Ni H, Liu J, Li X, Sha Z, Pu HAI (2021) An improved fractal permeability model for porous geomaterials with complex pore structures and rough surfaces. *Fractals* 30:2250002. <https://doi.org/10.1142/S0218348X22500025>
- Ning Y, Liu X, Kang Ge, Qi Lu (2022) Simulations of crack development in brittle materials under dynamic loading using the numerical manifold method. *Eng Fract Mech* 275:108830. <https://doi.org/10.1016/j.engfracmech.2022.108830>
- Ringel LM, Jalali M, Bayer P (2021) Stochastic inversion of three-dimensional discrete fracture network structure with hydraulic tomography. *Water Resour Res*. <https://doi.org/10.1029/2021WR030401>
- Sanderson DJ, Nixon CW (2018) Topology, connectivity and percolation in fracture networks. *J Struct Geol* 115:167–177. <https://doi.org/10.1016/j.jsg.2018.07.011>
- Sheng G, Yuliang Su, Wang W (2019) A new fractal approach for describing induced-fracture porosity/permeability/compressibility in stimulated unconventional reservoirs. *J Petrol Sci Eng* 179:855–866. <https://doi.org/10.1016/j.petrol.2019.04.104>
- Shi Di, Li L, Liu J, Mingyang Wu, Pan Y, Tang J (2022) Effect of discrete fractures with or without roughness on seepage characteristics of fractured rocks. *Phys Fluids* 34:073611. <https://doi.org/10.1063/5.0097025>
- Shi Di, Li L, Guo Y, Liu J, Tang J, Chang X, Song R, Mingyang Wu (2023) Estimation of rough fracture network permeability using fractal and topology theories. *Gas Sci Eng* 116:205043. <https://doi.org/10.1016/j.jgsce.2023.205043>
- Sun F, Huang W, Zhao B, Xue S, Zhou Bo (2023) Particle flow simulation of Brazilian splitting failure characteristics of layered shale. *J Pet Explor Prod Technol* 13:1865–1875. <https://doi.org/10.1007/s13202-023-01646-x>
- Wang Z, Bao Y, Pereira J-M, Sauret E, Gan Y (2022) Influence of multiscale surface roughness on permeability in fractures. *Phys Rev Fluids* 7:024101. <https://doi.org/10.1103/PhysRevFluids.7.024101>
- Witherspoon PA, Wang JS, Iwai K, Gale JE (1980) Validity of cubic law for fluid flow in a deformable rock fracture. *Water Resour Res* 16:1016–1024. <https://doi.org/10.1029/WR016i006p01016>
- Wu M, Wang W, Zhang D, Deng B, Liu S, Jun Lu, Luo Y, Zhao W (2020) The pixel crack reconstruction method: from fracture image to crack geological model for fracture evolution simulation. *Constr Build Mater* 273:121733. <https://doi.org/10.1016/j.conbuilmat.2020.121733>
- Wu M, Wang W, Shi Di, Song Z, Li M, Luo Y (2021) Improved box-counting methods to directly estimate the fractal dimension of a rough surface. *Measurement* 177:109303. <https://doi.org/10.1016/j.measurement.2021.109303>
- Wu M, Gao Ke, Liu J, Song Z, Huang X (2022) Influence of rock heterogeneity on hydraulic fracturing: a parametric study using the combined finite-discrete element method. *Int J Solids Struct* 234–235:111293. <https://doi.org/10.1016/j.ijsolstr.2021.111293>
- Wu M, Jiang C, Song R, Liu J, Li M, Liu B, Shi D, Zhu Z, Deng B (2023) Comparative study on hydraulic fracturing using different discrete fracture network modeling: insight from homogeneous to heterogeneity reservoirs. *Eng Fract Mech*. <https://doi.org/10.1016/j.engfracmech.2023.109274>
- Xia B, Luo Y, Huarui Hu, Mingyang Wu (2021) Fractal permeability model for a complex tortuous fracture network. *Phys Fluids* 33:096605. <https://doi.org/10.1063/5.0063354>
- Xu C, Dowd PA, Mardia KV, Fowell RJ (2006) A connectivity index for discrete fracture networks. *Math Geol* 38:611–634. <https://doi.org/10.1007/s11004-006-9029-9>
- Yang F, Wang F, Jiangmin Du, Yang S, Wen R (2023) Fractal characteristics of artificially matured lacustrine shales from Ordos Basin West China. *J Pet Explor Prod Technol* 13:1703–1713. <https://doi.org/10.1007/s13202-023-01637-y>
- Yang Yu, Wang D, Yang J, Wang B, Liu T (2021) Fractal analysis of CT images of tight sandstone with anisotropy and permeability prediction. *J Petrol Sci Eng* 205:108919. <https://doi.org/10.1016/j.petrol.2021.108919>
- Yao C, Shao Y, Yang J, Huang F, He C, Jiang Q, Zhou C (2020) Effects of fracture density, roughness, and percolation of fracture network on heat-flow coupling in hot rock masses with embedded three-dimensional fracture network. *Geothermics* 87:101846. <https://doi.org/10.1016/j.geothermics.2020.101846>
- Yu B, Li J (2011) Some fractal characters of porous media. *Fractals* 09:365–372. <https://doi.org/10.1142/S0218348X01000804>
- Zarin T, Sufali A, Ghaedi M (2023) Systematic comparison of advanced models of two- and three-parameter equations to model the imbibition recovery profiles in naturally fractured reservoirs. *J*

- Pet Explor Prod Technol 13:2125–2137. <https://doi.org/10.1007/s13202-023-01667-6>
- Zhang J, Ma G, Yang Z, Ma Q, Zhang W, Zhou W (2022) Investigation of flow characteristics of landslide materials through pore space topology and complex network analysis. *Water Resour Res* 58(9):e2021WR031735. <https://doi.org/10.1029/2021WR031735>
- Zhu J, Cheng Y (2018) Effective permeability of fractal fracture rocks: significance of turbulent flow and fractal scaling. *Int J Heat Mass Transf* 116:549–556. <https://doi.org/10.1016/j.ijheatmasstransfer.2017.09.026>
- Zhu W, Khirevich S, Patzek T (2021) Impact of fracture geometry and topology on the connectivity and flow properties of stochastic fracture networks. *Water Resour Res*. <https://doi.org/10.1029/2020WR028652>

Publisher's Note Springer Nature remains neutral with regard to jurisdictional claims in published maps and institutional affiliations.